

Boschelli, J., Moschetti, M. P., Sens-Schönfelder, C. (2021): Temporal Seismic Velocity Variations: Recovery Following From the 2019 Mw 7.1 Ridgecrest, California Earthquake. - Journal of Geophysical Research: Solid Earth, 126, 4, e2020JB021465.

<https://doi.org/10.1029/2020JB021465>

JGR Solid Earth

RESEARCH ARTICLE

10.1029/2020JB021465

Key Points:

- Seismic velocity changes due to the M_w 7.1 Ridgecrest earthquake have fundamentally altered the area within 30 km of the epicenter of the mainshock
- The maximum amplitude of the changes in seismic velocity exhibits strong correlations with log-distance and with peak dynamic strain suggesting that strong ground motion is among the primary cause of earthquake-induced seismic velocity changes
- Seismic velocity recovers asymptotically, approaching stable values between 1 and 3 months after the M_w 7.1 Ridgecrest earthquake

Supporting Information:

Supporting Information may be found in the online version of this article.

Correspondence to:

J. Boschelli,
joshua.boschelli@slu.edu

Citation:

Boschelli, J., Moschetti, M. P., & Sens-Schönfelder, C. (2021). Temporal seismic velocity variations: Recovery following from the 2019 M_w 7.1 Ridgecrest, California earthquake. *Journal of Geophysical Research: Solid Earth*, 126, e2020JB021465. <https://doi.org/10.1029/2020JB021465>

Received 30 NOV 2020

Accepted 8 MAR 2021

Published 2021. This article is a U.S. Government work and is in the public domain in the USA.

Temporal Seismic Velocity Variations: Recovery Following From the 2019 M_w 7.1 Ridgecrest, California Earthquake

Joshua Boschelli^{1,2} , Morgan P. Moschetti¹ , and Christoph Sens-Schönfelder³ 

¹Geological Hazards Science Center, U.S. Geological Survey, Golden, CO, USA, ²Department of Earth and Atmospheric Sciences, Saint Louis University, St. Louis, MO, USA, ³Helmholtz Centre Potsdam-GFZ German Research Centre for Geosciences, Potsdam, Germany

Abstract We investigated seismic velocity changes (dv/v) associated with the 2019 Ridgecrest earthquake sequence with high-frequency autocorrelations of ambient seismic noise data. Daily autocorrelation functions were computed for the entirety of 2019 and the first quarter of 2020 for broadband stations within the region, including the temporary broadband stations installed during the aftershock deployment. Travel time shifts in the daily autocorrelation functions, relative to the mean autocorrelation waveform, were computed to produce dv/v time series, which are sensitive to the evolving material properties of the shallow crust surrounding the Ridgecrest fault zone (RFZ). A short-term velocity drop follows the M_w 7.1 earthquake at stations in the vicinity of the rupture surface, while those greater than 50 km away showed no such drop. The maximum, absolute changes in seismic velocity are proportional to the logarithm of distance from the fault rupture and to the peak dynamic strain experienced during the earthquake. Near the areas of the highest coseismic slip within the RFZ, seismic velocities recovered over 3 months. However, in the vicinity of the nearby Garlock fault, where triggered slip manifested, and north of the RFZ, seismic velocities recovered within a month. We interpret the seismic velocity changes and their recovery to be largely due to changes in the physical properties of the shallow crust, such as fault zone damage recovery caused by the earthquake rupture process and in response to the large dynamic stresses of passing seismic waves from the mainshock.

1. Introduction

The earthquake rupture process and strong ground-shaking from large earthquakes cause permanent and transient effects on local seismic velocity within the shallow crust of the Earth. For example, Sawazaki et al. (2016) detected velocity decreases of 3.1% and 1.4% following the M_w 6.2 northern Nagano Prefecture earthquake, and Rivet et al. (2011) reported a velocity decrease of 0.2% during the M_w 7.5 Guerrero slow-slip event. Seismic velocities have been used to monitor changes within the crust, particularly using the coda portion of the seismic wavefield from earthquakes (Poupinet et al., 1984). Because the path lengths and travel time through a medium are greater for scattered waves than for direct waves, the seismic coda has an increased sensitivity to changes in the structure (Snieder, 2006; Wegler et al., 2006). In addition, temporal changes of coda wave properties resulting from earthquakes have also been studied using artificial explosions (Nishimura et al., 2000; Wegler et al., 2006). However, these are impractical in most cases due to earthquakes occurring irregularly and controlled explosions being limited in their application.

By eliminating the dependency on active sources or earthquakes, ambient seismic noise provides a way to continuously monitor subsurface properties. Using correlation functions between stations, or autocorrelations at a single station, it is possible to compute the seismic velocity changes from travel time perturbations in the coda of the correlation functions (Brennguier et al., 2008a, 2008b; Campillo & Paul, 2003; Shapiro et al., 2005). Recent developments have combined the theory of coda interferometry with passive seismic imaging. Assuming that the velocity change is uniform in space, the temporal change can be estimated from the phase shift between the functions and a reference correlation function of the time period in question. This study employs one such method called Passive Image Interferometry (PII) (Sens-Schönfelder & Wegler, 2006; Wegler & Sens-Schönfelder, 2007) using autocorrelations to examine the subsurface properties of the crust. Prior studies have shown that PII is sensitive to the changes in the shallow crust, furthering our

understanding into the mechanisms responsible for the time-evolution of crustal conditions following large magnitude earthquakes (Brenquier et al., 2008a, 2008b; Duputel et al., 2009; Mordret et al., 2010; Ohmi et al., 2008; Sens-Schönfelder & Wegler, 2011; Wegler & Lühr, 2001).

While the reduction of seismic velocities within the crust resulting from large magnitude earthquakes continues to be documented, the physical mechanisms and their effects are still under debate. Rubinstein and Beroza (2004a) discuss four different mechanisms for observed velocity changes. The first being that the change of the static stress results in positive and negative velocity shifts corresponding to regions of increased and decreased stress within a region (Hirose et al., 2017; Li et al., 2003a; Nishimura et al., 2000; Poupinet et al., 1984). Second, modification of existing hydrologic systems may change fluid content and pore pressure variations, thereby influencing seismic velocity (Jónsson et al., 2003; Minato et al., 2012; Yates et al., 2019). Third, the physical damage caused by fault motion could result in reduced velocities as the crust ruptures during the main shock and as cracks open and close in response to stress changes (Fielding et al., 2009; Karner et al., 1997; Li et al., 1998, 2003, 2006; Mordret et al., 2016; Olsen et al., 1998; Rubinstein et al., 2007; Taira & Brenquier, 2016; Tenthorey et al., 2003; Vidale & Li, 2003). Finally, near-surface physical damage caused by the nonlinearity of strong ground motion can cause velocity decreases. Changes are expected to be shallow and to correlate with the strength of shaking (Nakata & Snieder, 2011; Peng & Ben-Zion, 2006; Rubinstein & Beroza, 2004a, 2004b; Rubinstein et al., 2007; Schaff & Beroza, 2004).

In this study, we focus on the temporal changes of seismic velocity associated with the M_w 7.1 Ridgecrest earthquake, which occurred in the shallow crust north-northeast of the town of Ridgecrest, California, and west of Searles Valley, a region which accommodates one-quarter of the strain between the Pacific and North American plates (Frankel et al., 2008; Miller et al., 2001). We apply the PII techniques to continuous waveform data recorded by high-sensitivity seismograph stations for areas that experienced strong to severe ground-shaking to quantify the temporal variations of seismic velocity. We identify seismic velocity changes, compare the results at multiple stations to investigate their spatial and temporal relationships, and discuss the implications of the velocity changes observed along the RFZ and the Garlock fault.

2. Data

We collected continuous data from 36 broadband seismographs and short-period seismometers from the Southern California Seismic Network, including the permanent Southern California Seismic Network (CI), U.S. Geological Survey (GS), Plate Boundary (PB), and Portable Southern California Seismic Arrays (ZY) networks (Figure 1). Fifteen months of continuous seismic data, spanning all of 2019 and the first quarter of 2020, was collected from the permanent networks. Because the GS and ZY stations were deployed immediately after the M_w 7.1 earthquake, their coverage begins after the mainshock occurred; however, measurements from the temporary deployment provide useful constraints on the evolution of seismic velocities in the months following their installation, particularly at sites near the rupture (Albuquerque Seismological Laboratory, 1980; Cochran et al., 2020).

Processing of the seismic data consisted of windowing the three-component data into day-long segments, correcting for the instrument response, resampling to 20 Hz, and high-pass filtering with a 1-Hz filter corner. We selected this frequency range, because high-frequency waves have been identified to be better suited to revealing small time shifts (Wegler & Sens-Schönfelder, 2007). In addition, by focusing on higher frequencies, and under the assumption that surface waves predominate the recovered signal, the measurements are most sensitive to the top few kilometers in depth (Mao et al., 2019).

It is important to remove large deterministic phases in the seismograms, such as those caused by earthquakes or anthropogenic sources near the station, which may bias or corrupt the autocorrelations. To combat this, the day-long segments of data were first detrended and divided into hour-long segments, and a defined threshold value was used to mute the seismograms. If the data exceeded the threshold value, all values of the hour-long segment were set to zero. For the final computation, the threshold value was chosen to be three times the standard deviation. After removing the effects of the earthquakes as described above, an autocorrelation across the six combinations of the individual components (E-E, N-N, Z-Z, E-N, E-Z, N-Z) were computed from the hour-long records, normalized, and combined to produce daily autocorrelations for each individual station.

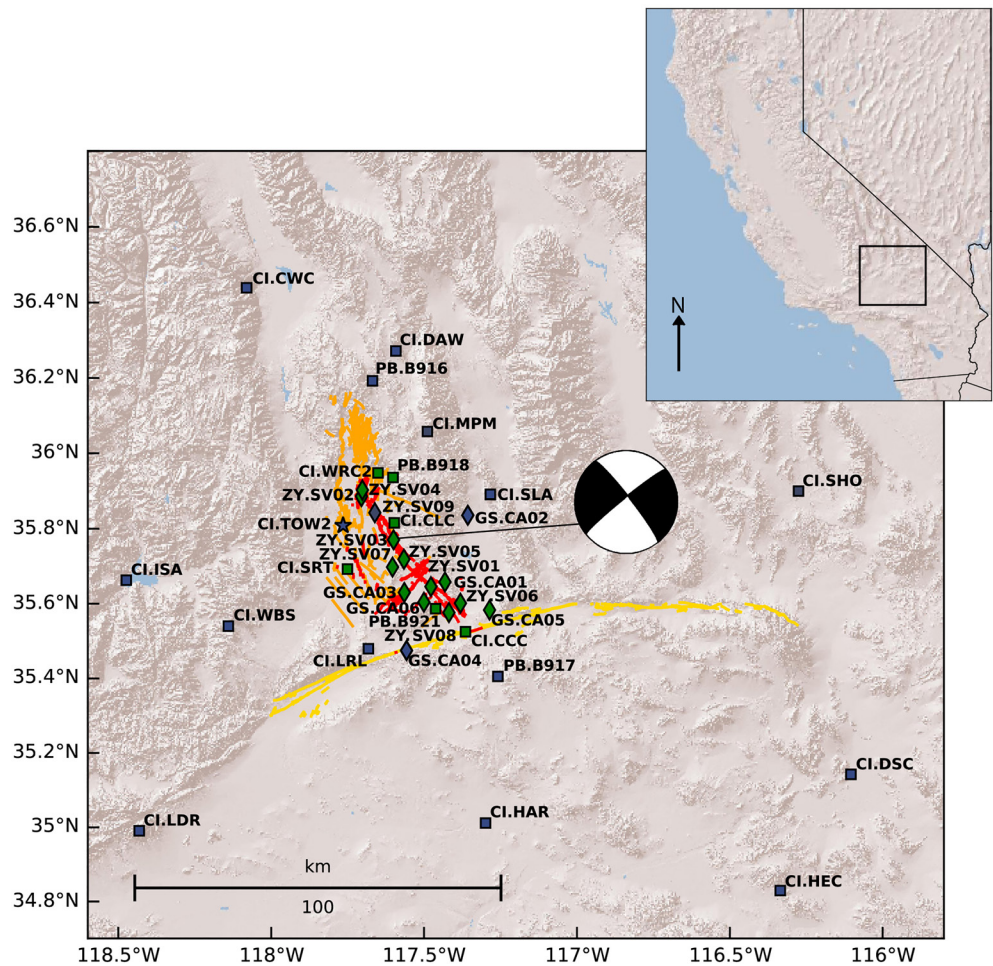


Figure 1. Locations of the permanent (square) and temporary (diamond) seismic stations relative to the M_w 7.1 Ridgecrest earthquake with the local fault network shown, the Ridgecrest fault zone (orange) and the Garlock fault (yellow) and the observed surface rupture (red). Stations that experienced a velocity change associated with the Ridgecrest earthquake are indicated in green, while those that did not are shown in navy. Stations that exhibit a strong correlation with thermoelastic strain are indicated with a star.

3. Methods

3.1. Passive Image Interferometry

To quantify the temporal variation of the seismic velocity, we adopt the techniques of Passive Image Interferometry as pioneered by Sens-Schönfelder and Wegler (2006). Sens-Schönfelder and Wegler (2006) showed that relative travel time variations can be determined for different lag-time windows in the calculated correlation functions. The relative travel time variations are calculated by computing a reference autocorrelation Φ_{ref} , which is the mean of all available daily autocorrelations, at each station for each of the component combinations. The autocorrelations, Φ , are then stretched and compressed, with respect to zero lag time, for stretching factors, ϵ , spanning from -2% to 2% . Wegler et al. (2009) clearly illustrate the time-stretching calculation. Estimates of dt/t from this time-stretching method have been demonstrated to yield more stable results (Hadziioannou et al., 2009) compared to sliding-window-type methods, such as the moving cross-spectral (MWCS) analysis (Poupinet et al., 1984). We selected the stretching factors, $\epsilon(t)$, that maximizes the daily correlation coefficient, $C(\epsilon, t)$ to represent the travel time fluctuation for each autocorrelation function over the lapse time window $[\tau_1, \tau_2]$

$$C(\varepsilon, t) = \frac{\int_{\tau_1}^{\tau_2} \Phi_{ref}(\tau(1 + \varepsilon)) \Phi(t, \tau) d\tau}{\left(\int_{\tau_1}^{\tau_2} \Phi_{ref}^2(\tau(1 + \varepsilon)) d\tau \int_{\tau_1}^{\tau_2} \Phi^2(t, \tau) d\tau \right)^{\frac{1}{2}}} \quad (1)$$

With the assumption that the velocity change is uniform in space, the dv/v measurements are related to the time shifts by

$$\varepsilon(t) = \frac{\Delta t}{t} = \frac{-dv}{v} \quad (2)$$

We performed this procedure for the daily autocorrelation constructed from the various component combinations. In order to quantify the uncertainty in the dv/v measurements for each day, we divided the day-length window into multiple nonoverlapping time windows. We computed dv/v from the multiple time windows across each combination and calculated the mean and standard deviation of these values.

3.2. Combing Multiple Components

The processing yields the temporal variation in seismic velocity, $\varepsilon_n(t)$, for each of the six unique combinations, n , of the recorded components of ground motion. Since the coda comprises highly scattered seismic waves, and the different combinations may contain scattered Rayleigh and Love waves, we combined the curves to gain an overall sensitivity to the surface waves propagating through the medium. Following from Hobiger et al. (2012), we compute weighted averages of the six component-based velocity variation curves, $\varepsilon_n(t)$, and the associated correlation coefficients by

$$\varepsilon(t) = \frac{\sum_{i=1}^n C_n^2(t) \cdot \varepsilon_n(t)}{\sum_{i=1}^n C_n^2(t)} \quad (3)$$

The associated correlation coefficient for each station is reported as

$$C(t) = \frac{\sum_{i=1}^n C_n^3(t)}{\sum_{i=1}^n C_n^2(t)} \quad (4)$$

By definition, the correlation coefficient associated with the averaged seismic velocity variation curves is less than or equal to the correlation coefficient of the highest correlation coefficient traces. We note, however, that the traces with the highest correlation received higher weights in the weighted averaging. Traces with larger variations in seismic velocity show lower correlation coefficients because the waveforms experience greater stretching factors, and these deviations from the reference waveform affect waveform similarity metrics.

4. Results

4.1. Temporal Evolution of the Autocorrelation Waveforms

Matrices of the daily autocorrelations provide initial information on the effect of the M_w 7.1 Ridgecrest earthquake at different stations. Figure 2 shows the records of CI.CLC and CI.HAR from January to September 2019, where each line represents a daily autocorrelation and is colored based on their correlation coefficient to the stacked, averaged correlation. The solid line marks the occurrence of the M_w 7.1 Ridgecrest earthquake. Before the earthquake, the autocorrelations from each station are relatively consistent, with only minor variations occurring. However, in the case of CI.CLC, once the earthquake occurs, the waveforms are distorted and the areas surrounding the central pulse of the stacked waveform become diminished. This diminished nature continues to be apparent in the days following the earthquake, with the autocorrelation eventually reverting to its premainshock state within 1 month. In contrast, for station CI.HAR, the autocorrelations remain fairly consistent, showing little to no evidence of the earthquake occurring.

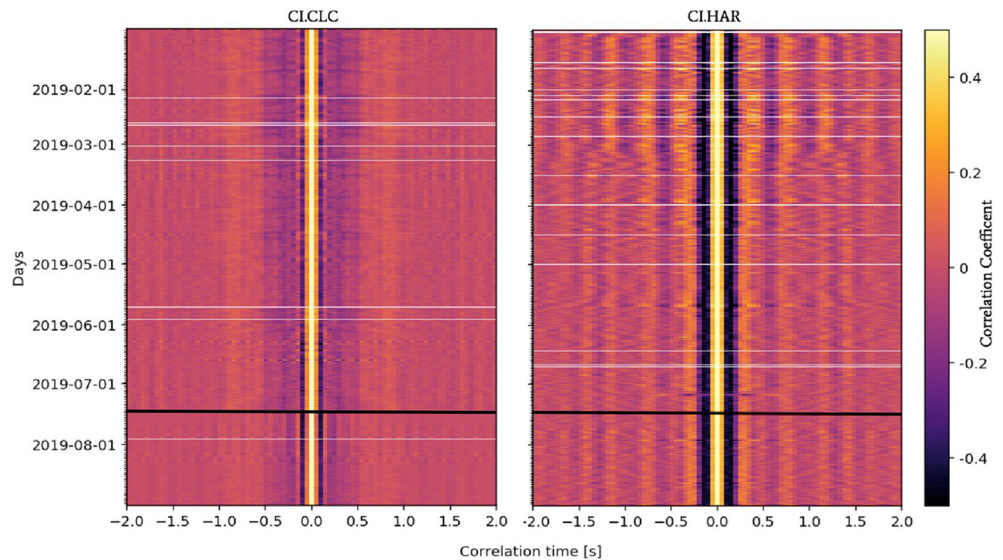


Figure 2. Stack of hourly autocorrelations for stations CI.CLC and CI.HAR. Color coded based on correlation coefficient between the daily correlations and the average correlations spanning from January to September 2019. The solid black line represents the M_w 7.1 Ridgecrest earthquake, while white lines represent missing data.

A similar trend was observed by Obermann et al. (2015), where fluid injections caused a loss of waveform coherence and was thought to be tied to changes of the scattering properties in the medium.

4.2. Sensitivity of the Autocorrelation to the Muting Threshold and Reference Stack

To diminish the effect of earthquakes and other transient signals in the calculation of autocorrelations, we used a defined threshold value to mute the seismograms. We tested the effect on the dv/v time series using a threshold of one, two, and three times the standard deviation for muting. Decreasing the factors of the standard deviation in the muting calculation has the effect of removing more data from the autocorrelation calculations. Figure S1 shows the velocity variations for stations CI.SHO and CI.CLC that result from varying the factor on the standard deviation value for applying muting. Besides a small degree of variation, the curves are highly similar, suggesting that the value of the factor on the standard deviation does not have a strong effect on the resulting autocorrelation, at least for the data set in question and for the muting factors investigated in this study.

As previously stated, the dv/v measurements are calculated by comparing the daily autocorrelations to a reference stack. This stack is meant to provide a stable point of comparison for the daily autocorrelations. We tested the effect of a reference stack that was formed from the full 15-months stack, from the first three months (Jan-Mar) of 2019, and from the last three months (Oct-Dec) of 2019. This was aimed at understanding the effect of any earthquakes that occurred before or after the Ridgecrest earthquake had on the dv/v values. Figure S2 shows the velocity variations for stations CI.MPM and CI.SRT that result from these three reference stacks. Besides a small degree of variation, the curves are highly similar, suggesting that the observed velocity variations are not highly dependent on the time window used for the reference stack and that the use of different time stacks for the reference stack gives similar results.

4.3. Temporal Seismic Velocity Variations

Among the 36 stations that were examined in this study, we observed varying temporal responses of seismic velocities in the coda of the autocorrelations to the M_w 7.1 Ridgecrest earthquake. Eighteen stations experienced dv/v change that coincided with the earthquake (Figure 3). For the permanent stations, we measured the velocity change by the difference between before and after the earthquake. For the stations of the aftershock deployment, we computed the maximum dv/v as the difference between the values at the earliest

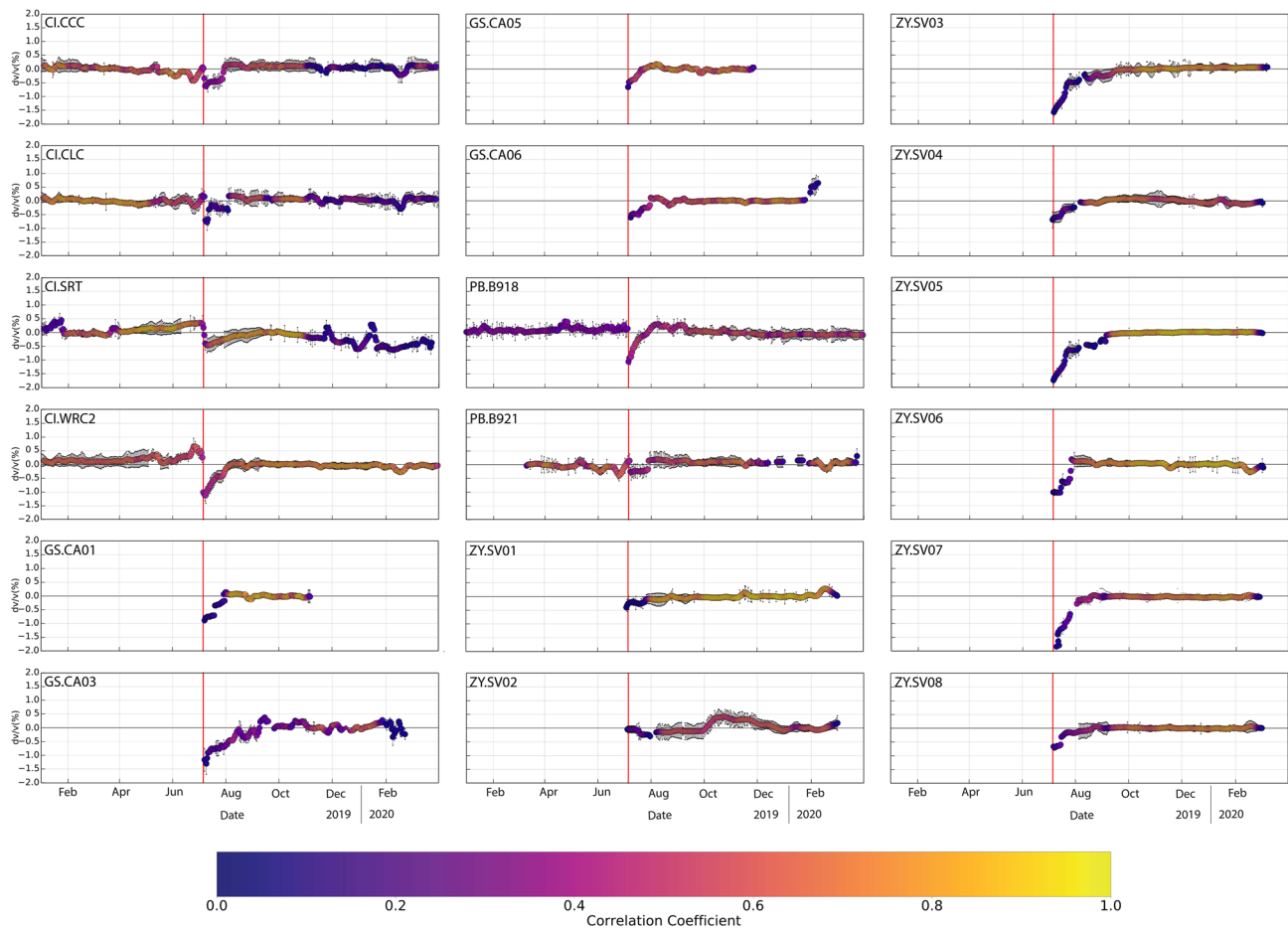


Figure 3. The temporal variations in seismic velocity (dv/v) for the 18 permanent and temporary stations that experienced a velocity drop associated with the M_w 7.1 Ridgecrest earthquake. Colors represent the correlation coefficients of the daily and reference autocorrelations, with their associated standard deviation shown. The red vertical line represents the M_w 7.1 Ridgecrest earthquake.

time available, and 1 month after the dv/v values stabilized. The maximum dv/v measurements from the aftershock deployments are presumably lower-bound estimates, because the measurements from permanent stations indicate that maximum dv/v changes immediately followed the M_w 7.1 Ridgecrest earthquake.

Six of the permanent stations experienced maximum velocity changes of -1.3% to -0.4% , relative to the dv/v values immediately before the M_w 7.1 Ridgecrest earthquake. Of the remaining 15 stations (CI.CWC, CI.DAW, CI.DSC, CI.HAR, CI.HEC, CI.ISA, CI.LDR, CI.LRL, CI.MPM, CI.SHO, CI.SLA, CI.TOW2, CI.WBS, PB.B916, and PB.B917) the dv/v time series either showed no perceptible response to the earthquake, remained relatively consistent over the time period, or exhibited a high level of background dv/v variation that made it impossible to identify changes associated with the Ridgecrest earthquake, Figure S3. For the temporary stations, all but three (GS.CA02, GS.CA04, and ZY.SV09), showed dv/v increasing from a minimum after the earthquake until the values finally stabilized. Both GS.CA02 and ZY.SV09 had deployment issues causing their data availability to be limited (Cochran et al., 2020). While the temporary stations were not installed at the time of the Ridgecrest earthquake and therefore could not record the immediate dv/v effects, they do exhibit the lasting effect of the mainshock on seismic velocity structure.

The correlation coefficients largely reflect the seismic velocity changes recorded at the different stations. On average, the stations that recorded larger changes in seismic velocity exhibit lower correlation coefficients, compared to stations that recorded smaller changes in the seismic velocity, due to the effects of waveform stretching on waveform correlation. We find a relationship between the correlation coefficient and the magnitude of the standard deviation. On days for which the correlation coefficient is high; the standard

deviation is lower than the standard deviations associated with days for which the correlation coefficients are low. This observation is explained by the fundamental properties of the stretch method, such that when the daily autocorrelation is similar to the reference stack, the range of stretch factors that will maximize the value will be low. While we see higher standard deviations following the earthquake, the observed seismic velocity drops exceed these uncertainty estimates and provide confidence in the main observations.

Variations in the dv/v appears limited to the M_w 7.1 Ridgecrest earthquake and is not observed for other earthquakes that occurred during the sequence. The Ridgecrest earthquake sequence included an M_w 6.4 foreshock, which occurred about 34 h before the M_w 7.1, as well as multiple $M_w > 5$ aftershocks that occurred in the months following the mainshock. Stations CI.CCC, CI.CLC, CI.SRT, CI.WRC2, PB.B918, and PB.B921 operated over the duration of the sequence and did not exhibit velocity changes following the M_w 6.4 earthquake. Furthermore, the temporary stations from the ZY network, which included multiple stations deployed within the RFZ, did not exhibit further velocity reductions resulting from earthquakes in the aftershock sequence, suggesting that these events did not cause seismic velocity perturbations or that the perturbations were below the resolution of this study (Figure S4).

For the six permanent stations that had observable velocity changes, two recovery periods were observed, with dv/v values recovered to background levels within multiple months. The seismic velocity at stations CI.SRT recovered to a stable level after about three months. In contrast, stations CI.CCC, CI.CLC, CI.WRC2, PB.B918, and PB.B921 saw their velocities recover within about 1 month after the Ridgecrest earthquake. The difference in recovery time correlates well with those stations further from the rupture, with recovery being slower nearer the rupture. In addition, the temporary stations dv/v curves took two months to stabilize following from the Ridgecrest earthquake. The longer recovery time appears to follow a steady dv/v increase over time period, while the 1-month recovery did not initiate until late in the process, and recovery occurred over a short time period.

4.4. Distance and Ground-Motion Dependence of the Seismic Velocity Variations

To explore whether correlations existed between the maximum dv/v changes, distance to the fault rupture, and the available earthquake ground-motion data, we compiled and computed the relevant metrics. We obtained estimates of the closest distances to the M_w 7.1 Ridgecrest finite-rupture surface from Rekoske et al. (2020). For the broadband instruments that were colocated with accelerometers, we extracted ground motions (peak horizontal ground acceleration and velocity) from the earthquake ground motion study of Rekoske et al. (2020). For the stations that lacked accelerometer recordings and for those that were installed following the M_w 7.1 earthquake, we used the U.S. Geological Survey ShakeMap inferences on ground motion at each site (Guy et al., 2015). We followed the methodology of Hill et al. (1993) and van der Elst and Brodsky (2010) in calculating the peak dynamic strains by dividing the peak ground velocity (PGV) by the local shear-wave velocity at each of the individual sites. Following Taira et al. (2015), we used the time-averaged shear velocity to a depth of 30 m (V_{s30}) (Wald & Allen, 2007) as a proxy for the local shear-wave velocity.

The maximum velocity changes show a strong positive correlation with the distance to the rupture surface (Rrup) (Figure 4a) and show larger decreases in dv/v closer to the fault rupture surface than at greater distances.

Comparisons of peak ground motions with the seismic velocity changes indicate a negative correlations with ground acceleration and the local site conditions at the stations with respect to the mainshock. Plots of the peak dynamic strain and dv/v measurements (Figure 4b) show a correlation with greater velocity changes at the sites that experienced higher peak dynamic strains than at sites with lower peak strains. The observed trend with respect to peak horizontal ground accelerations (PGA) indicate greater velocity changes at the sites that experienced stronger shaking (Figure S5). However, variance is high for the sites that experienced the strongest ground motions (PGA > 40% g), and some sites exhibit anomalously small seismic velocity changes despite having experienced strong ground motions (e.g., CI.TOW2).

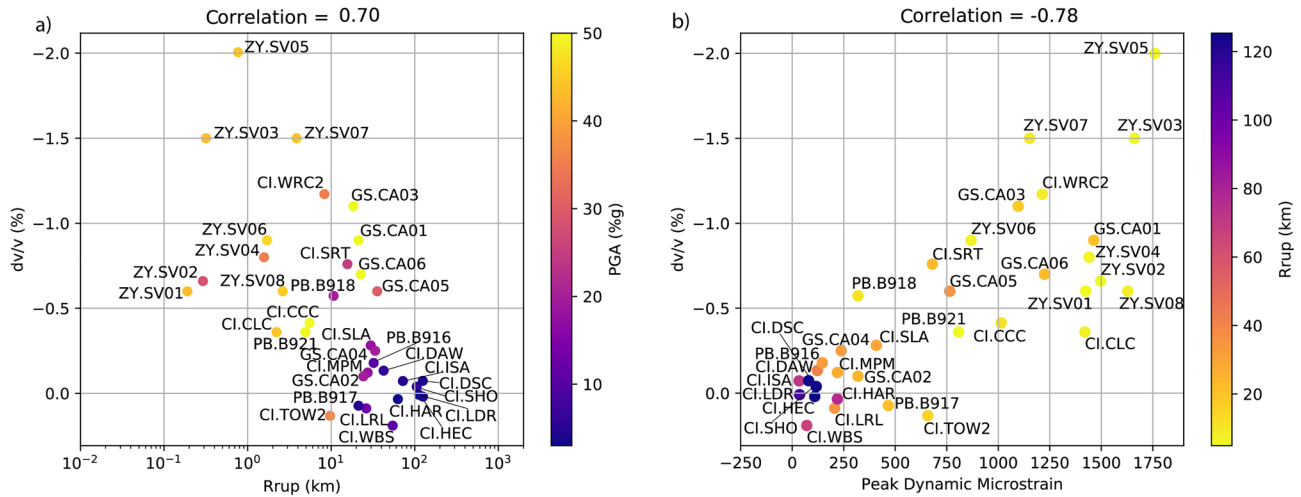


Figure 4. Scatterplot of the station parameters used in this study. (a) Scatterplot of the temporal velocity variations (dv/v) for the 35 stations used in this study, with ZY.SV09 excluded, as function of the closet distance to the rupture surface (Rrup). (b) Scatterplot of the temporal velocity variations (dv/v) as a function of peak dynamic microstrain.

4.5. Thermoelastic Strain Correlation With the Seismic Velocity Variations

While the majority of the stations in the vicinity of the Ridgecrest earthquake demonstrated an observable velocity change, two did not. ZY.SV09 had installation issues, leaving CI.TOW2 as the only outlier (Figure 5). Since the trend appears to be seasonal there are a wide variety of geophysical processes that could be at play. These include rain and other hydrologic phenomena (e.g., Hainzl et al., 2006; King et al., 1994; Roeloffs, 2001), loadings due to changes in atmospheric pressure (Christiansen et al., 2005), ocean swells (e.g., Kedar et al., 2008; Schulte-Pelkum et al., 2004), thermoelastic strain (e.g., Ben-Zion & Leary, 1986; Berger, 1975), and other mechanisms listed in Dong et al. (2002). Since the mainshock occurred in the vicinity of the Naval Air Weapon Station China Lake, the available environmental data are limited to daily surface temperature measurements. For this reason, we choose to investigate the effects of thermoelastic strain on the temporal variations of the dv/v measurements.

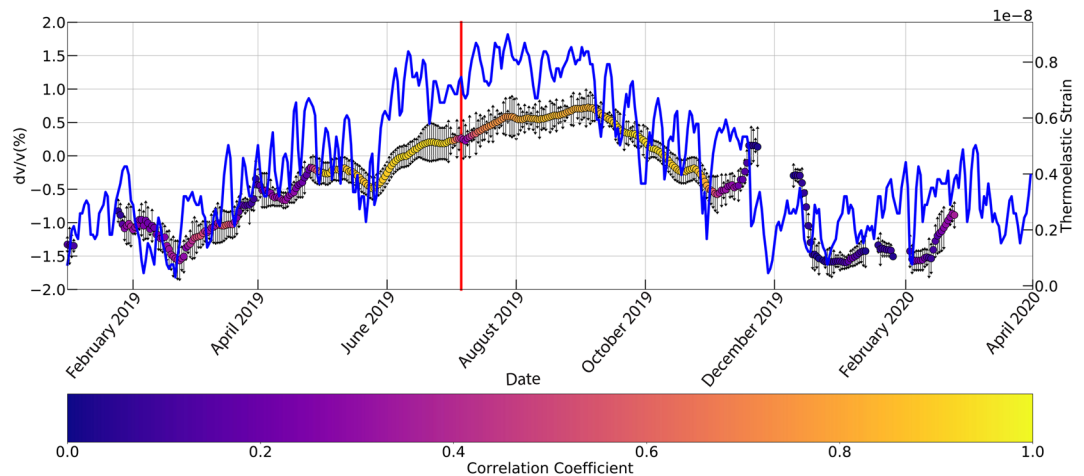


Figure 5. The temporal variations in seismic velocity (dv/v) for CI.TOW2. The calculated thermoelastic strain is shown in blue. Colors represent the correlation coefficients of the daily and reference autocorrelations, with their associated standard deviation shown in black. The red vertical line represents the M_w 7.1 Ridgecrest earthquake.

Following Ben-Zion and Allam (2013), we calculated the strain induced at depth by surface temperature changes using the methodology of Ben-Zion and Leary (1986). Ben-Zion and Allam (2013) found that the surface temperature field is assumed to be given by a standing wave of the form

$$T(x, y = 0, t) = \sum_{\omega} T_{\omega} \cos(kx) e^{i(\omega t - \phi)} \quad (5)$$

where x is horizontal distance, y is depth, ω is the angular frequency, $T_{\omega} = \sqrt{A_{\omega}^2 + B_{\omega}^2}$ denoting the amplitudes of the sine and cosine components of the temporal spectral decomposition, $\phi = \tan^{-1}(A_{\omega} / B_{\omega})$, and $k = 2\pi / \lambda$ is the wavenumber of the standing temperature field with wavelength λ . Using Equation 5 as a surface boundary, the horizontal thermoelastic strain component ε_{xx} in a homogeneous elastic half-space can be written from the solution of Berger (1975) as

$$\varepsilon_{xx} = \sum_{\omega} \left(\frac{1 + \sigma}{1 - \sigma} \right) \left(\frac{k}{\gamma + k} \right) \left(\left[2\{1 - \sigma\} + \frac{k}{\gamma - k} - ky \right] e^{-ky} - \frac{k}{\gamma - k} e^{-\gamma y} \right) \left(\beta T_{\omega} \cos(kx) e^{i(\omega t - \phi)} \right) \quad (6)$$

where $\gamma = k \left[1 + \frac{i\omega}{\kappa k^2} \right]^{1/2}$, κ is the thermal diffusivity coefficient, β is the coefficient of linear thermal expansion, and σ is Poisson's ratio. Following from Ben-Zion and Allam (2013), we found that the direct substitution of the recorded surface temperature of our area of interest can be used to satisfy the temperature component of Equation 5 to provide a rough estimate. To further model the thermoelastic strain, we set $\beta = 8 \times 10^{-5} \text{ } ^\circ\text{C}^{-1}$, $\kappa = 1.6 \cdot 10^{-2} \text{ m}^2 / \text{day}$ and $\sigma = 0.3$, to model granite, assuming it to represent the bulk composition of the shallow continental crust.

We find a strong correlation between the phasing of the dv/v time series and the thermoelastic strains at station CI.TOW2. If the large dv/v fluctuations are due to thermoelastic effects, any dv/v changes due to the Ridgecrest earthquake may be obscured by these environmental signals in the autocorrelations. Why these effects would be so significant at CI.TOW2 is unclear at this time. Ben-Zion and Leary (1986) suggested that regions with laterally heterogeneous material properties may show these effects to a greater degree. Features of the thermoelastic strain effects may also be observed at other stations, with reduced amplitudes, including the decreasing trend in dv/v (October 2019 to April 2020) at CI.SRT and the upward-trending dv/v values immediately preceding the Ridgecrest earthquake sequence, such as are observed at stations CI.SRT and CI.WRC2.

5. Discussion

We examined the correlation between the seismic velocity changes resulting from the Ridgecrest earthquake and peak dynamic strains to compare the predictive metrics. Because the maximum changes in seismic velocity correlate with both distance to the rupture surface and with the peak dynamic strains experienced from the M_w 7.1 Ridgecrest earthquake, the cause of these dv/v changes cannot be inferred from the correlations alone. Taira et al. (2015) similarly found a correlation between the observed velocity change and peak dynamic strain for the South Napa earthquake, but the dv/v changes are close to an order of magnitude lower than what was observed in this study, for similar values of the peak dynamic microstrain. Because differences in the data processing and measurement details between Taira et al. (2015) and this study may have significant effects on the measured dv/v changes, we also examined the predicted peak dynamic microstrains from the M_w 6.4 Ridgecrest earthquake (Figure S6). We computed peak dynamic microstrains from the M_w 6.4 at the sites of the permanent stations. Based on the values the observed dv/v measurements for the M_w 6.4 would be on the same order for the stations that did not have any noticeable reaction to the M_w 7.1 earthquake. This may explain why the seismic velocity changes shown in this study show no evidence of the M_w 6.4 foreshock as shown in Figure S4. However, the weaker correlation with PGA indicates that sites experiencing stronger ground motions ($>40\%$ g) preferentially show experience reduced seismic velocities when the local shear-wave velocities are lower than at sites with higher local shear-wave velocities.

The correlation between the observed temporal velocity changes, peak ground acceleration, and peak dynamic strains between the M_w 6.4 and M_w 7.1 Ridgecrest earthquakes, and between the measurements of this study and from the M_w 6.0 South Napa earthquake (Taira et al., 2015) indicate that strong ground motion is among the primary cause of earthquake-induced seismic velocity changes. Hobiger et al. (2016) observed a similar trend and concluded that while the two values certainly play an important role in the explanation of the coseismic velocity changes, they ultimately cannot explain the coseismic velocity changes. Our findings support this explanation and may explain why the M_w 6.4 earthquake or other aftershocks in the sequence did not have noticeable, large-scale effects on the temporal velocity changes. Furthermore, of the four possible mechanisms discussed by Rubinstein and Beroza (2004a) our results support all but the first, since we do not observe positive and negative velocity shifts associated with the mainshock. Additional investigation will be needed to narrow down the mechanisms further.

6. Conclusion

In this study, we investigated the temporal change and spatial patterns of the seismic velocity associated with the M_w 7.1 Ridgecrest earthquake. We computed daily autocorrelations, for all six cross-components, and identified travel time variations in the waveforms. Evidence of changes in the seismic travel times is apparent in the autocorrelation matrices (Figure 2) and in the seismic velocity variations that were computed by waveform stretching calculations on the coda waves (Figure 3). Time series of the seismic velocity changes indicate that the area near the Ridgecrest fault zone and the Garlock fault experienced months-long modifications to the seismic velocity structure, with substantial recovery within multiple months. The maximum seismic velocity changes correlate with peak dynamic strains from the M_w 7.1 earthquake and with the distance to the rupture surface. The observed drop in seismic velocity is assumed to be caused by the modification of the subsurface through the opening of new cracks, fault zone damage and dilation, near-surface effects, or modifications of the stress field near the fault. The effects appear to be most strongly localized near the fault and within the fault zone, and the amplitude of the dynamic stress field appears to have an influence on the long-term reductions in seismic velocity. Results from post-earthquake investigation of site characterization, hydrogeologic modifications, and inferred and direct measurements of stress, including seismologically observed stress drops and borehole breakout observations, would provide additional insight into the causative mechanisms for the seismic velocity changes.

Data Availability Statement

Seismograms used in this study were collected using ObsPy, an open-source project dedicated to providing a Python framework for processing seismological data. The data used in this study were obtained from the Southern California Earthquake Data Center (SCEDC) at www.scedc.caltech.edu/research-tools and the IRIS Data Management Center at www.iris.edu under network codes CI (<https://doi.org/10.17914/SN/CI>), GS (<https://doi.org/10.7914/SN/GS>), PB, and ZY (last accessed September 2020). The surface temperature data were obtained from the National Oceanic and Atmospheric Administrations (NOAA) Climate database, <https://www.ncdc.noaa.gov/cdo-web/search>. The individual station parameters (PGA, PGV, and Rrup) were measured from the U.S. Geological Survey ShakeMap, <https://earthquake.usgs.gov/earthquakes/eventpage/ci3845/shakemap/pga>, while the Vs30 values were measured using the U.S. Geological Survey Vs30 Map viewer app, <https://usgs.maps.arcgis.com/apps/webappviewer/index.html?id=8ac19b-c334f747e486550f32837578e1>. The values for Rrup were obtained from Rekoske et al. (2020). The data processing and measurements in this study were made using the Monitoring and Imaging based on Interferometric concepts package (www.github.com/miic-sw/miic). Figures were made using Matplotlib, a Python 2D plotting library, www.matplotlib.org (Hunter, 2007).

References

- Albuquerque Seismological Laboratory (ASL)/USGS. (1980). *U.S. Geological Survey Network, International Federation of Digital Seismograph Networks*. <https://doi.org/10.7914/SN/GS>
- Ben-Zion, Y., & Allam, A. A. (2013). Seasonal thermoelastic strain and postseismic effects in Parkfield borehole dilatometers. *Earth and Planetary Science Letters*, 379, 120–126. <https://doi.org/10.1016/j.epsl.2013.08.024>

Acknowledgments

We thank Elizabeth Cochran, Yehuda Ben-Zion, Nori Nakata along with the two anonymous reviewers for their helpful discussions and suggestions. Elizabeth Cochran reviewed an early version of this manuscript. This work was partially supported by the Earthquake Hazards Program of the U.S. Geological Survey.

- Ben-Zion, Y., & Leary, P. (1986). Thermoelastic strain in a half-space covered by unconsolidated material. *Bulletin of the Seismological Society of America*, 76(5), 1447–1460.
- Berger, J. (1975). A note on thermoelastic strains and tilts. *Journal of Geophysical Research*, 80(2), 274–277. <https://doi.org/10.1029/JB080i002p00274>
- Brenguier, F., Campillo, M., Hadziioannou, C., Shapiro, N. M., Nadeau, R. M., & Larose, E. (2008a). Postseismic relaxation along the San Andreas fault at Parkfield from continuous seismological observations. *Science*, 321(5895), 1478–1481. <https://doi.org/10.1126/science.1160943>
- Brenguier, F., Shapiro, N. M., Campillo, M., Ferrazzini, V., Duputel, Z., Coutant, O., & Nercessian, A. (2008b). Towards forecasting volcanic eruptions using seismic noise. *Nature Geoscience*, 1(2), 126–130. <https://doi.org/10.1038/ngeo104>
- California Institute of Technology and United States Geological Survey Pasadena. (1926). *Southern California Seismic Network*. International Federation of Digital Seismograph Networks. <https://doi.org/10.7914/SN/CI>
- Campillo, M., & Paul, A. (2003). Long-range correlations in the diffuse seismic coda. *Science*, 299(5606), 547–549. <https://doi.org/10.1126/science.1078551>
- Christiansen, L., Hurwitz, S., Saar, M., Ingebritsen, S., & Hsieh, P. (2005). Seasonal seismicity at western United States volcanic centers. *Earth and Planetary Science Letters*, 240(2), 307–321. <https://doi.org/10.1016/j.epsl.2005.09.012>
- Cochran, E. S., Wolin, E., McNamara, D. E., Yong, A., Wilson, D., Alvarez, M., et al. (2020). The U.S. Geological Survey's rapid seismic array deployment for the 2019 Ridgecrest earthquake sequence. *Seismological Research Letters*, 91(4), 1952–1960. <https://doi.org/10.1785/0220190296>
- Dong, D., Fang, P., Bock, Y., Cheng, M. K., & Miyazaki, S. (2002). Anatomy of apparent seasonal variations from GPS-derived site position time series. *Journal of Geophysical Research*, 107(B4), 2075. <https://doi.org/10.1029/2001JB000573>
- Duputel, Z., Ferrazzini, V., Brenguier, F., Shapiro, N., Campillo, M., & Nercessian, A. (2009). Real time monitoring of relative velocity changes using ambient seismic noise at the Piton de la Fournaise volcano (La Réunion) from January 2006 to June 2007. *Journal of Volcanology and Geothermal Research*, 184(1–2), 164–173. <https://doi.org/10.1016/j.jvolgeores.2008.11.024>
- Fielding, E. J., Lundgren, P. R., Bürgmann, R., & Funning, G. J. (2009). Shallow fault-zone dilatancy recovery after the 2003 Bam earthquake in Iran. *Nature*, 458(7234), 64–68. <https://doi.org/10.1038/nature07817>
- Frankel, K. L., Glazner, A. F., Kirby, E., Monastero, F. C., Strane, M. D., Oskin, M. E., et al. (2008). Active tectonics of the eastern California shear zone. In *Field guide to plutons, volcanoes, faults, reefs, dinosaurs, and possible glaciation in selected area of Arizona, California, and Nevada* (Vol. 11, pp. 43–81). Geological Society of America Field Guide. [https://doi.org/10.1130/2008.fld011\(03\)](https://doi.org/10.1130/2008.fld011(03))
- Guy, M. R., Patton, J. M., Fee, J., Hearne, M., Martinez, E., Ketchum, D., et al. (2015). *National Earthquake Information Center systems overview and integration*. U.S. Department of the Interior, U.S. Geological Survey.
- Hadziioannou, C., Larose, E., Coutant, O., Roux, P., & Campillo, M. (2009). Stability of monitoring weak changes in multiply scattering media with ambient noise correlation: Laboratory experiments. *The Journal of the Acoustical Society of America*, 125(6), 3688–3695. <https://doi.org/10.1121/1.3125345>
- Hainzl, S., Kraft, T., Wassermann, J., Igel, H., & Schmedes, E. (2006). Evidence for rainfall-triggered earthquake activity. *Geophysical Research Letters*, 33, L19303. <https://doi.org/10.1029/2006GL027642>
- Hill, D. P., Reasenber, P. A., Michael, A., Arabaz, W. J., Beroza, G., Brumbaugh, D., et al. (1993). Seismicity remotely triggered by the magnitude 7.3 Landers, California, Earthquake. *Science*, 260(5114), 1617–1623. <https://doi.org/10.1126/science.260.5114.1617>
- Hirose, T., Nakahara, H., & Nishimura, T. (2017). Combined use of repeated active shots and ambient noise to detect temporal changes in seismic velocity: Application to Sakurajima volcano, Japan. *Earth, Planets and Space*, 69, 42. <https://doi.org/10.1186/s40623-017-0613-7>
- Hobiger, M., Wegler, U., Shiomi, K., & Nakahara, H. (2012). Coseismic and postseismic elastic wave velocity variations caused by the 2008 Iwate-Miyagi Nairiku earthquake, Japan. *Journal of Geophysical Research*, 117, B09313. <https://doi.org/10.1029/2012JB009402>
- Hobiger, M., Wegler, U., Shiomi, K., & Nakahara, H. (2016). Coseismic and post-seismic velocity changes detected by Passive Image Interferometry: Comparison of one great and five strong earthquakes in Japan. *Geophysical Journal International*, 205(2), 1053–1073. <https://doi.org/10.1093/gji/ggw066>
- Hunter, J. D. (2007). Matplotlib: A 2D graphics environment. *Computing in Science and Engineering*, 9(3), 90–95. <https://doi.org/10.1109/MCSE.2007.55>
- Jónsson, S., Segall, P., Pedersen, R., & Björnsson, G. (2003). Post-earthquake ground movements correlated to pore-pressure transients. *Nature*, 424(6945), 179–183. <https://doi.org/10.1038/nature01776>
- Karner, S. L., Marone, C., & Evans, B. (1997). Laboratory study of fault healing and lithification in simulated fault gouge under hydrothermal conditions. *Tectonophysics*, 277(1–3), 41–55. [https://doi.org/10.1016/S0040-1951\(97\)00077-2](https://doi.org/10.1016/S0040-1951(97)00077-2)
- Kedar, S., Longuet-Higgins, M., Webb, F., Graham, N., Clayton, R., & Jones, C. (2008). The origin of deep ocean microseisms in the North Atlantic Ocean. *Proceedings of the Royal Society A*, 464(2091), 777–793. <https://doi.org/10.1098/rspa.2007-27710.1098/rspa.2007.0277>
- King, G. C., Stein, R. S., & Lin, J. (1994). Static stress changes and the triggering of earthquakes. *Bulletin of the Seismological Society of America*, 84(3), 935–954.
- Li, Y.-G., Chen, P., Cochran, E. S., Vidale, J. E., & Burdette, T. (2006). Seismic evidence for rock damage and healing on the San Andreas Fault associated with the 2004 Mw 6.0 Parkfield earthquake. *Bulletin of the Seismological Society of America*, 96(4B), S349–S363. <https://doi.org/10.1785/0120050803>
- Li, Y.-G., Vidale, J. E., Aki, K., Xu, F., & Burdette, T. (1998). Evidence of shallow fault zone strengthening after the 1992 Mw 7.5 landers, California, earthquake. *Science*, 279(5348), 217–219. <https://doi.org/10.1126/science.279.5348.217>
- Li, Y.-G., Vidale, J. E., Day, S. M., Oglesby, D. D., & Cochran, E. (2003a). Postseismic fault healing on the rupture zone of the 1999 Mw 7.1 Hector Mine, California, earthquake. *Bulletin of the Seismological Society of America*, 93(2), 854–869. <https://doi.org/10.1785/0120020131>
- Mao, S., Campillo, M., Hillst, R. D., Brenguier, F., Stehly, L., & Hillers, G. (2019). High temporal resolution monitoring of small variations in crustal strain by dense seismic arrays. *Geophysical Research Letters*, 46, 128–137. <https://doi.org/10.1029/2018GL079944>
- Miller, M. M., Johnson, D. J., Dixon, T. H., & Dokka, R. K. (2001). Refined kinematics of the eastern California shear zone from GPS observations, 1993–1998. *Journal of Geophysical Research*, 106(B2), 2245–2263. <https://doi.org/10.1029/2000JB000328>
- Minato, S., Tsuji, T., Ohmi, S., & Matsuoka, T. (2012). Monitoring seismic velocity change caused by the 2011 Tohoku-oki earthquake using ambient noise records. *Geophysical Research Letters*, 39, L09309. <https://doi.org/10.1029/2012GL051405>
- Mordret, A., Jolly, A. D., Duputel, Z., & Fournier, N. (2010). Monitoring of phreatic eruptions using interferometry on retrieved cross-correlation function from ambient seismic noise: Results from Mt. Ruapehu, New Zealand. *Journal of Volcanology and Geothermal Research*, 191(1–2), 46–59. <https://doi.org/10.1016/j.jvolgeores.2010.01.010>
- Mordret, A., Mikesell, T. D., Harig, C., Lipovsky, B. P., & Prieto, G. A. (2016). Monitoring southwest Greenland's ice sheet melt with ambient seismic noise. *Science Advances*, 2(5), e1501538. <https://doi.org/10.1126/sciadv.1501538>

- Nakata, N., & Snieder, R. (2011). Near-surface weakening in Japan after the 2011 Tohoku-Oki earthquake. *Geophysical Research Letters*, *38*, L17302. <https://doi.org/10.1029/2011GL048800>
- Nishimura, T., Uchida, N., Sato, H., Ohtake, M., Tanaka, S., & Hamaguchi, H. (2000). Temporal changes of the crustal structure associated with the M6.1 earthquake on September 3, 1998, and the volcanic activity of Mount Iwate, Japan. *Geophysical Research Letters*, *27*(2), 269–272. <https://doi.org/10.1029/1999GL005439>
- Obermann, A., Kraft, T., Larose, E., & Wiemer, S. (2015). Potential of ambient seismic noise techniques to monitor the St. Gallen geothermal site (Switzerland). *Journal of Geophysical Research: Solid Earth*, *120*, 4301–4316. <https://doi.org/10.1002/2014JB011817>
- Ohmi, S., Hirahara, K., Wada, H., & Ito, K. (2008). Temporal variations of crustal structure in the source region of the 2007 Noto Hanto earthquake, central Japan, with passive image interferometry. *Earth, Planets and Space*, *60*, 1069–1074. <https://doi.org/10.1186/BF03352871>
- Olsen, M. P., Scholz, C. H., & Léger, A. (1998). Healing and sealing of a simulated fault gouge under hydrothermal conditions: Implications for fault healing. *Journal of Geophysical Research*, *103*(B4), 7421–7430. <https://doi.org/10.1029/97JB03402>
- Peng, Z., & Ben-Zion, Y. (2006). Temporal changes of shallow seismic velocity around the Karadere-Düzce branch of the North Anatolian fault and strong ground motion. *Pure and Applied Geophysics*, *163*(2–3), 567–600. <https://doi.org/10.1007/s00024-005-0034-6>
- Poupinet, G., Ellsworth, W. L., & Frechet, J. (1984). Monitoring velocity variations in the crust using earthquake doublets: An application to the Calaveras Fault, California. *Journal of Geophysical Research*, *89*(B7), 5719–5731. <https://doi.org/10.1029/JB089iB07p05719>
- Rekoske, J. M., Thompson, E. M., Moschetti, M. P., Hearne, M. G., Aagaard, B. T., & Parker, G. A. (2020). The 2019 Ridgecrest, California, earthquake sequence ground motions: Processed records and derived intensity metrics. *Seismological Research Letters*, *91*(4), 2010–2023. <https://doi.org/10.1785/0220190292>
- Rivet, D., Campillo, M., Shapiro, N. M., Cruz-Atienza, V., Radiguet, M., Cotte, N., & Kostoglodov, V. (2011). Seismic evidence of nonlinear crustal deformation during a large slow slip event in Mexico. *Geophysical Research Letters*, *38*, L08308. <https://doi.org/10.1029/2011GL047151>
- Roeloffs, E. A. (2001). Creep rate changes at Parkfield, California 1966–1999: Seasonal, precipitation induced, and tectonic. *Journal of Geophysical Research*, *106*(B8), 16525–16547. <https://doi.org/10.1029/2001JB000352>
- Rubinstein, J. L., & Beroza, G. C. (2004a). Evidence for widespread nonlinear strong ground motion in the MW 6.9 Loma Prieta earthquake. *Bulletin of the Seismological Society of America*, *94*(5), 1595–1608. <https://doi.org/10.1785/012004009>
- Rubinstein, J. L., & Beroza, G. C. (2004b). Nonlinear strong ground motion in the ML5.4 Chittenden earthquake: Evidence that preexisting damage increases susceptibility to further damage. *Geophysical Research Letters*, *31*, L23614. <https://doi.org/10.1029/2004GL021357>
- Rubinstein, J. L., Uchida, N., & Beroza, G. C. (2007). Seismic velocity reductions caused by the 2003 Tokachi-Oki earthquake. *Journal of Geophysical Research*, *112*, B05315. <https://doi.org/10.1029/2006JB004440>
- Sawazaki, K., Saito, T., Ueno, T., & Shiomi, K. (2016). Estimation of seismic velocity changes at different depths associated with the 2014 Northern Nagano Prefecture earthquake, Japan (Mw 6.2) by joint interferometric analysis of NIED Hi-net and KiK-net records. *Progress in Earth and Planetary Science*, *3*(1), 36. <https://doi.org/10.1186/s40645016-0112-710.1186/s40645-016-0112-7>
- Schaff, D. P., & Beroza, G. C. (2004). Coseismic and postseismic velocity changes measured by repeating earthquakes. *Journal of Geophysical Research*, *109*, B10302. <https://doi.org/10.1029/2004JB003011>
- Schulte-Pelkum, V., Earle, P. S., & Vernon, F. L. (2004). Strong directivity of ocean-generated seismic noise. *Geochemistry, Geophysics, Systems*, *5*, Q03004. <https://doi.org/10.1029/2003GC000520>
- Sens-Schönfelder, C., & Wegler, U. (2006). Passive image interferometry and seasonal variations of seismic velocities at Merapi Volcano, Indonesia. *Geophysical Research Letters*, *33*, L21302. <https://doi.org/10.1029/2006GL027797>
- Sens-Schönfelder, C., & Wegler, U. (2011). Passive image interferometry for monitoring crustal changes with ambient seismic noise. *Comptes Rendus Geoscience*, *343*(8), 639–651. <https://doi.org/10.1016/j.crte.2011.02.005>
- Shapiro, N. M., Campillo, M., Stehly, L., & Ritzwoller, M. H. (2005). High-resolution surface-wave tomography from ambient seismic noise. *Science*, *307*(5715), 1615–1618. <https://doi.org/10.1126/science.1108339>
- Snieder, R. (2006). The theory of coda wave interferometry. *Pure and Applied Geophysics*, *163*(2–3), 455–473. <https://doi.org/10.1007/s00024-005-0026-6>
- Taira, T. A., & Brenguier, F. (2016). Response of hydrothermal system to stress transients at Lassen Volcanic Center, California, inferred from seismic interferometry with ambient noise. *Earth, Planets and Space*, *68*, 162. <https://doi.org/10.1186/s40623-016-0538-6>
- Taira, T. A., Brenguier, F., & Kong, Q. (2015). Ambient noise-based monitoring of seismic velocity changes associated with the 2014 Mw 6.0 South Napa earthquake. *Geophysical Research Letters*, *42*, 6997–7004. <https://doi.org/10.1002/2015GL065308>
- Tenthorey, E., Cox, S. F., & Todd, H. F. (2003). Evolution of strength recovery and permeability during fluid-rock reaction in experimental fault zones. *Earth and Planetary Science Letters*, *206*(1), 161–172. [https://doi.org/10.1016/S0012-821X\(02\)01082-8](https://doi.org/10.1016/S0012-821X(02)01082-8)
- van der Elst, N. J., & Brodsky, E. E. (2010). Connecting near-field and far-field earthquake triggering to dynamic strain. *Journal of Geophysical Research*, *115*, B07311. <https://doi.org/10.1029/2009JB006681>
- Vidale, J. E., & Li, Y.-G. (2003). Damage to the shallow Landers fault from the nearby Hector Mine earthquake. *Nature*, *421*(6922), 524. <https://doi.org/10.1038/nature01354>
- Wald, D. J., & Allen, T. I. (2007). Topographic slope as a proxy for seismic site conditions and amplification. *Bulletin of the Seismological Society of America*, *97*(5), 1379–1395. <https://doi.org/10.1785/0120060267>
- Wegler, U., & Lühr, B.-G. (2001). Scattering behaviour at Merapi volcano (Java) revealed from an active seismic experiment. *Geophysical Journal International*, *145*(3), 579–592. <https://doi.org/10.1046/j.1365-246x.2001.01390.x>
- Wegler, U., Lühr, B.-G., Snieder, R., & Ratdomopurbo, A. (2006). Increase of shear wave velocity before the 1998 eruption of Merapi volcano (Indonesia). *Geophysical Research Letters*, *33*, L09303. <https://doi.org/10.1029/2006GL025928>
- Wegler, U., Nakahara, H., Sens-Schönfelder, C., Korn, M., & Shiomi, K. (2009). Sudden drop of seismic velocity after the 2004 Mw 6.6 mid-Niigata earthquake, Japan, observed with passive image interferometry. *Journal of Geophysical Research*, *114*, B06305. <https://doi.org/10.1029/2008JB005869>
- Wegler, U., & Sens-Schönfelder, C. (2007). Fault zone monitoring with passive image interferometry. *Geophysical Journal International*, *168*(3), 1029–1033. <https://doi.org/10.1111/j.1365-246X.2006.03284.x10.1111/j.1365-246x.2006.03284.x>
- Yates, A. S., Savage, M. K., Jolly, A. D., Caudron, C., & Hamling, I. J. (2019). Volcanic, coseismic, and seasonal changes detected at white island (Whakaari) volcano, New Zealand, using seismic ambient noise. *Geophysical Research Letters*, *46*, 99–108. <https://doi.org/10.1029/2018GL080580>